Synthetic Aperture Focusing of Ultrasonic Data From Multilayered Media Using an Omega-K Algorithm

Martin H. Skjelvareid, *Student Member, IEEE*, Tomas Olofsson, Yngve Birkelund, *Member, IEEE*, and Yngvar Larsen, *Member, IEEE*

***Abstract*—The synthetic aperture focusing technique (SAFT) is used to create focused images from ultrasound scans. SAFT has traditionally been applied only for imaging in a single medium, but the recently introduced phase shift migration (PSM) algorithm has expanded the use of SAFT to multilayer structures. In this article we present a similar focusing algorithm called multi-layer omega-k (MULOK), which combines PSM and the ω-k algorithm to perform multilayer imaging more efficiently. The asymptotic complexity is shown to be lower for MULOK than for PSM, and this is confirmed by comparing execution times for implementations of both algorithms. To facilitate the complexity analysis, a detailed description of algorithm implementation is included, which also serves as a guide for readers interested in practical implementation. Using data from an experiment with a multilayered structure, we show that there is essentially no difference in image quality between the two algorithms.**

I. Introduction

Synthetic aperture processing is used in radar, sonar, seismic, and ultrasound imaging. The technique is based on emitting a wave into a region of interest, recording the backscattered echoes, and repeating this for several positions. Recorded data are subsequently combined to create a large synthetic aperture, yielding a high-resolution image of the reflectivity in the region.

Synthetic aperture imaging is in many ways similar to imaging using arrays of multiple transmitters and/or receivers. Although there are several advantages to using such arrays, they do not offer any increase in resolution compared with monostatic synthetic aperture imaging [1], [2]. Because monostatic imaging systems also have low complexity, cost, and spatial requirements, they remain relevant in modern applications.

Within the field of seismic imaging, synthetic aperture techniques are known as migration techniques. Computer-based processing of seismic data started in the 1970s [3], and the initial methods were limited to time-space domain processing. In 1978, Stolt [4] introduced what is now called the frequency-wavenumber, or ω-k, algorithm, performing all processing in the temporal frequency and spatial frequency domains. This approach proved to be significantly faster than the other methods available at the time, and it has since become widely used in many related fields. Its main disadvantage is that it requires the wave velocity of the propagating medium to be constant. In the same year, Gazdag [5] introduced the phase shift migration (PSM) algorithm, which also operates in the frequency-wavenumber domain. Although PSM is not as fast as the ω-k algorithm, it allows the wave velocity to vary with depth.

Both the ω-k and the PSM algorithm are based on extrapolating the backscattered wavefield from the plane in which it is recorded down into the region to be imaged. In Fourier analysis of wave fields, this is also known as angular spectrum propagation [6], [7].

Building on previous work within sonar and radar imaging, synthetic aperture focusing was introduced to the field of NDT ultrasonics in the 1970s, and came to be known as the synthetic aperture focusing technique (SAFT) [8]. Although the time-domain delay-and-sum method was the starting point, frequency domain algorithms were soon adopted by the ultrasonic community, yielding low execution times at the cost of increased memory usage [9]–[13]. In recent years, there has also been a growing interest in adapting such algorithms for arrays [14], [15]. Researchers have mainly focused on imaging in a single, constant-velocity medium, but some time-domain methods for multilayer structures have been developed [16], [17], and recently Olofsson [18] introduced the use of the frequency-domain PSM algorithm for processing multilayer data. In this article, we combine the PSM and ω-k algorithms to create a more efficient multilayer algorithm, and extend the experimental setup to include three-layered media.

There are several applications for ultrasound imaging of multilayer structures. One very important case is that of immersion scans, in which an object is immersed in water and several pulse-echo measurements are performed by scanning the transducer in the water layer above the object. The water and the object constitutes a two-layer structure, and to properly focus the backscattered echoes from within the object, the focusing algorithm has to take the wave velocities of both media into account. This is also the case for other multi-layered structures, for example, steel pipes lined with a corrosion-resistant layer.

Manuscript received November 18, 2010; accepted February 22, 2011. The authors thank Breivoll Inspection Technologies and the Research Council of Norway for funding this work.

M. H. Skjelvareid and Y. Birkelund are with the University of Tromsø, Department of Physics and Technology, Tromsø, Norway (e-mail: martin.skjelvareid@breivoll.no).

T. Olofsson is with Uppsala University, Department of Engineering Sciences, Uppsala, Sweden.

Y. Larsen is with Norut, the Northern Research Institute, Department of Earth Observation, Tromsø, Norway.

Digital Object Identifier 10.1109/TUFFC.2011.1904

The main advantages of immersion scans, as opposed to contact scans, are that the water layer acts as a good and uniform couplant for the acoustic waves, and that there is no friction to cause transducer wear. The transducer used in immersion scans is usually geometrically focused to provide a good lateral resolution in the transducer focal zone. Synthetic aperture techniques represent an alternative that can be used to obtain a high lateral resolution that is independent of depth.

As previously mentioned, the ω-k algorithm has proven to be very efficient for single-layer processing, and the PSM algorithm is capable of imaging structures where the wave velocity varies with depth. In 1989, Kim [19] introduced a method for seismic imaging which combines the advantages of both algorithms. He assumed that the geological structure of the earth can be approximated as a finite number of layers with constant wave velocity and used the PSM algorithm to extrapolate the wavefield down to the interfaces between the layers. He then used the ω-k algorithm to effectively image the interior of each layer. In this paper, we demonstrate that the same approach can be used for ultrasonic imaging of multilayer structures, and we will refer to this as the multi-layer omega-k algorithm (MULOK). The algorithm is compared with the PSM algorithm in terms of both computational complexity and image quality.

To simplify the treatment of the algorithms, a two-dimensional geometry is considered here, but an extension to three dimensions is straightforward. A real ultrasound application is usually three-dimensional in nature, but if the region of interest is homogenous along one direction, a two-dimensional approximation can be made without any loss of information.

To compare the asymptotical complexity of the PSM and MULOK algorithms, a detailed description of the algorithm implementations has been included. As an added benefit, the description also serves as a guide for practical implementation.

The remainder of this article is organized as follows: In Section II, the theories of the PSM and MULOK algorithms are presented, and in Section III, the asymptotic complexity of each algorithm is analyzed and compared with actual execution times. An experiment illustrating the imaging performance of both algorithms is presented in Section IV, before we state our conclusions in Section V. Details of algorithm implementation and complexity analysis have been placed in the Appendix, to maintain the flow of the article for the general reader.

II. Theory

A. The Exploding Reflector Model

Derivation of migration algorithms for the monostatic case are often based on the exploding reflector model [20], [21], which simplifies the inverse imaging problem. It reduces the two-way pulse-echo scenario to a one-way scenario in which we assume that the scatterers themselves are sources of acoustic energy.

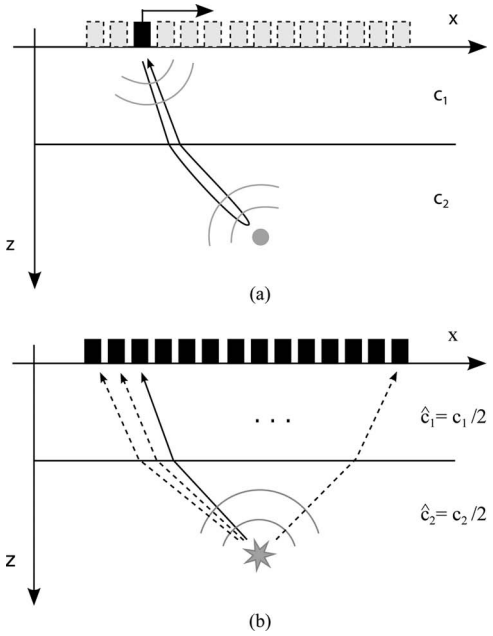

Fig. 1. (a) Scanned pulse-echo measurements and (b) the exploding reflector model.

Fig. 1 illustrates a B-scan of a two-layer geometry, where a transducer is scanned along the x-axis and a pulse-echo measurement is performed for each x position. A scatterer is present in the second layer, and because the two layers have different wave velocities, both the transmitted and the reflected wave are refracted at the interface between the layers.

Fig. 1 shows how the exploding reflector model is applied to the same geometry. The scatterer is assumed to spontaneously radiate a wave which travels toward an array of transducer positions, undergoing the same refraction as for the pulse-echo case. In order for the time delay of the pulses to remain the same under the exploding reflector model as for the actual pulse-echo measurement, an effective wave velocity of half the actual velocity must be assumed,

$$\hat{c}_l = \frac{c_l}{2}, \tag{1}$$

where l is the layer index. The model is general and can be applied for an arbitrary number of layers.

In most ultrasonic measurements, there are multiple reflectors, and the wave field measured by the transducer is then approximated as a superposition of waves from several exploding reflectors. This assumption holds true as long as multiple reflections between scatterers can be neglected.

B. Extrapolation of Wave Fields in the Fourier Domain

For migration algorithms, the purpose of wave field extrapolation is to calculate the wave field at an arbitrary

depth from measurements performed at a given depth, here denoted Z. In the following derivation we will assume that all scatterers are located in the half-space $z > Z$.

Let $p(t, x, z)$ denote the wave field generated by a set of exploding reflectors, and assume that only longitudinal waves are present in the medium. The shear wave components of the wave field can generally be ignored if the medium is not a solid, or if the waves have a near-normal incidence angle at interfaces to solids, as is often the case in immersion scans.

Assume now that the wave field is recorded along the line $z = Z$, so that $p(t, x, Z)$ is known. Note that because all scatterers are assumed to be located in the half-space $z > Z$, all recorded waves are traveling in the negative z direction. The Fourier transform of the recorded wave field is given by

$$P(\omega, k_x, Z) = \frac{1}{4\pi^2} \iint_{-\infty}^{+\infty} p(t, x, Z) e^{-i(k_x x - \omega t)} \mathrm{d}x \mathrm{d}t, \quad (2)$$

where $1/(4\pi^2)$ is a normalization constant. It can be shown [7] that the wave field can be extrapolated to any depth $Z + \Delta z$ by multiplication with a complex exponential,

$$P(\omega, k_x, Z + \Delta z) = P(\omega, k_x, Z) \cdot e^{ik_z(\omega, k_x) \cdot \Delta z}, \quad (3)$$

where $k_z(\omega, k_x)$ is given by

$$k_z(\omega, k_x) = -\mathrm{sgn}(\omega) \cdot \sqrt{\frac{\omega^2}{\hat{c}^2} - k_x^2}. \quad (4)$$

The sign function ensures that the k_z value represents a wave traveling in the negative z direction, and the effective wave velocity $\hat{c} = c/2$ is used because the exploding reflector model is assumed. An inverse Fourier transform is used to obtain the extrapolated wave field in time-space coordinates,

$$p(t, x, Z + \Delta z) = \iint_{-\infty}^{+\infty} P(\omega, k_x, Z) e^{ik_z \Delta z} e^{i(k_x x - \omega t)} \mathrm{d}k_x \mathrm{d}\omega. \quad (5)$$

C. Imaging Condition

Given an expression for the wave field $p(t, x, z)$, an imaging condition is needed to obtain an image $I(x,z)$ of the exploding reflectors. For the exploding reflector model, the imaging condition is to set $t = 0$ [21], so that

$$I(x, z) = p(t = 0, x, z). \quad (6)$$

The wave field emitted from a scatterer is maximally concentrated in space at the origin of the time axis, and thus the imaging condition in (6) is chosen to produce a maximally focused image.

D. Imaging Using Phase Shift Migration

Applying the imaging condition of (6) to (5), we get

$$I(x, Z + \Delta z) = \iint_{-\infty}^{+\infty} P(\omega, k_x, Z) e^{ik_z \Delta z} e^{ik_x x} \mathrm{d}k_x \mathrm{d}\omega. \quad (7)$$

Note that inserting $t = 0$ into (5) reduces the inverse transform with respect to ω to a simple integral over ω. Eq. (7) can be used iteratively to create an image line by line, by applying it for all depths $Z + \Delta z$ to be imaged. In seismic processing, this is called phase shift migration (PSM), referring to the phase shift given by the term $e^{ik_z \Delta z}$.

E. Imaging Through Stolt Transform

Eq. (7) is very similar to an inverse Fourier transform of $P(\omega, k_x, Z)$, but it has an $e^{ik_z \Delta z}$ kernel rather than an $e^{-i\omega t}$ kernel. It can be recast into a proper inverse Fourier transform by a change of variables from ω to k_z. Integrals in the form of Fourier transforms are of particular interest, as they can be calculated using the computationally efficient fast Fourier transform (FFT) and its inverse counterpart (IFFT).

We obtain an expression for ω by using the relation given in (4), and assuming, as in Section II-B, that ω and k_z have opposite signs, so that

$$\omega(k_z, k_x) = -\mathrm{sgn}(k_z) \cdot \hat{c} \sqrt{k_x^2 + k_z^2}. \quad (8)$$

By substituting (8) into (7), we get

$$I(x, Z + \Delta z) = \iint_{-\infty}^{+\infty} P(k_z, k_x, Z) e^{ik_z \Delta z} e^{ik_x x} \mathrm{d}k_x \mathrm{d}k_z, \quad (9)$$

where

$$P(k_z, k_x, Z) = A(k_z, k_x) \cdot P(\omega(k_x, k_z), k_x, Z), \quad (10)$$

and

$$A(k_z, k_x) = \frac{\partial \omega(k_z, k_x)}{\partial k_z} = \frac{\hat{c}}{\sqrt{1 + \frac{k_x^2}{k_z^2}}}. \quad (11)$$

We see here that, relative to the original wave field $P(\omega, k_x, Z)$, the substitution of variables leads to a multiplication with an amplitude factor $A(k_z, k_x)$ and a shift in ω given by $\omega(k_z, k_x)$.

F. Adaptation to Multilayer Case

Assume now that we have several layers with potentially different wave velocities, as shown in Fig. 2. Let the layers be numbered with $l = 1, 2, \ldots, L$, and let d_l and c_l denote the thickness and wave velocity of layer l, respectively. The top of the uppermost layer is denoted Z_1, and the interfaces between the layers are denoted Z_l, so that the top of layer l is given by $Z_l = Z_1 + \sum_{m=1}^{l-1} d_m$.

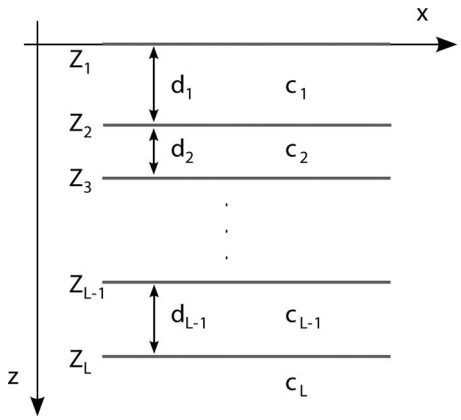

Fig. 2. Illustration of horizontally layered geometry.

We know from (3) that in a medium with constant sound speed, the wave field $P(\omega, k_x, Z)$ can be calculated by multiplying a reference wave field $P(\omega, k_x, Z)$ with a phase factor $e^{ik_z\Delta z}$. In the multilayer case, the field cannot be extrapolated through several layers directly, because k_z is a function of the medium velocity $\hat{c}_l$,

$$k_{zl} = -\mathrm{sgn}(\omega)\cdot\sqrt{\frac{\omega^2}{\hat{c}_l^2} - k_x^2}, \tag{12}$$

where the layer dependence is indicated by index l. However, extrapolation within each layer is still possible,

$$P(\omega, k_x, Z_l + \Delta z) = P(\omega, k_x, Z_l)\cdot e^{ik_{zl}\Delta z}, \quad \Delta z < d_l, \tag{13}$$

where $P(\omega, k_x, Z_l)$ denotes the field at interface Z_l, and $P(\omega, k_x, Z_l + \Delta z)$ denotes the field at depth $z = Z_l + \Delta z$.

If the wave field is to be extrapolated to more than one layer, the transmission of waves through the layer interfaces has to be considered. The transmission factor between different media is generally a complex function, dependent on both incident angle and the acoustic impedances of the media [22]. However, for most commonly available ultrasound transducers, the directivity of the transducer limits the emitted and received wave fields to a relatively small angle interval. We will therefore assume that the transmission factors are approximately independent of incident angle, so that the wave fields directly above and directly below an interface are proportional;

$$P(\omega, k_x, Z_l^-) \propto P(\omega, k_x, Z_l^+), \tag{14}$$

where the plus and minus signs are used to indicate the upper and lower side of the interface, respectively. Because we are mainly interested in relative amplitudes within each layer, the amplitude scaling effect imposed by the interfaces is considered here to be unimportant to the imaging problem.

Assuming proportionality across interfaces, the wave field at an arbitrary interface Z_l can, within a scaling factor, be calculated from the wave field measured at Z_1,

$$P(\omega, k_x, Z_l) \propto P(\omega, k_x, Z_1)\cdot e^{i\sum_{m=1}^{l} k_{zm} d_m}. \tag{15}$$

Eqs. (13) and (15) constitute the basis for PSM imaging of several layers. The imaging procedure for layer l can be summarized as follows:

1) Calculate the wave field at the top of the layer interface, $P(\omega, k_x, Z_l)$, using (15).
2) For each depth $Z_l + \Delta z$ to be imaged within the layer:
   a) Shift the wave field downwards with Δz by multiplying with a phase factor, according to (13), to obtain $P(\omega, k_x, Z_l + \Delta z)$.
   b) Create an image line $I(x, Z_l + \Delta z)$ by integrating with regard to ω and inverse transforming with regard to k_x, according to (7).

Instead of creating an image of each layer line by line, the Stolt transform introduced in Section II-E can be adapted to the multilayer case to enable imaging of an entire layer through a single inverse Fourier transform. This is the approach we call MULOK. The complete image for layer l is then given by

$$I_l(x, \Delta z) = \iint_{-\infty}^{+\infty} P(k_z, k_x, Z_l) e^{-ik_z\Delta z} e^{ik_x x}\,\mathrm{d}k_x\,\mathrm{d}k_z, \quad \Delta z < d_l, \tag{16}$$

where

$$P(k_z, k_x, Z_l) = A_l(k_z, k_x)\cdot P_l(\omega_l(k_x, k_z), k_x, Z_l), \tag{17}$$

$$A_l(k_z, k_x) = \frac{\hat{c}_l}{\sqrt{1 + \frac{k_x^2}{k_{zl}^2}}}, \text{and} \tag{18}$$

$$\omega_l(k_z, k_x) = -\mathrm{sgn}(k_{zl})\cdot\hat{c}_l\sqrt{k_x^2 + k_{zl}^2}. \tag{19}$$

The imaging procedure to create an image of layer l can be summarized in the following way:

1) Calculate the wave field at the top of the layer, $P(\omega, k_x, Z_l)$, using (15).
2) Use (17)–(19) to perform the variable transformation from ω to k_{zl}.
3) Inverse transform to obtain the image within the layer, $I_l(x, \Delta z)$, using (16).

G. Comments on Theoretical Resolution

The lateral resolution of a synthetic aperture image is dependent on the bandwidth of the k_x spectrum [23], and this bandwidth is limited by the effective length L of the transducer. A common rule of thumb for the single-layer case is that this makes the maximum lateral resolution approximately $L/2$ [13]. Here we will argue that this limit is also relevant for the multilayer case.

According to Snell's law, the k_x wavenumber of a wave incident on a layer interface must remain the same after transmission into the next medium. Thus, the refraction of the wave does not in itself alter the horizontal wavenumber, but the transmission factors between media are generally dependent on incident angle, making the interface a filter for the k_x spectrum. The bandwidth of the k_x spectrum is only maintained as long as the transmission factors are approximately uniform within the divergence angle of the transducer, but in practice, this requirement is fulfilled for many transducer designs and material combinations of interest. For example, for an immersion scan of copper using a 2.25-MHz, 10-mm-diameter transducer, the echo transmission factor varies by only approximately 6% within the transducer beam [18]. As long as the k_x spectrum bandwidth can be assumed to be the same for the single-layer and multilayer case, the theoretical lateral resolution of $L/2$ is also the same.

III. Algorithmic Complexity

A. Asymptotic Complexity

The effectiveness of an algorithm is often quantified by analyzing how the number of operations grows as the size of the input data tends toward infinity, and this asymptotic complexity is denoted using big-O notation. In the case of the PSM and MULOK algorithms, the size of the input data are given by the number of time samples, N, the number of measurement positions, M, and the number of layers, L. Note that the sampling frequency is assumed to be constant, so that the number of frequency samples within the transducer bandwidth is proportional to the number of time samples. The asymptotic complexities for each individual step of the algorithms are analyzed in part E of the Appendix, and are listed in Tables I and II. The overall complexity of each algorithm is given by the algorithm step with the highest-order complexity. To analyze this, we consider the complexities with regard to N, M, and L separately, assuming that the two remaining variables are kept constant. The highest-order complexities are summarized in Table III. MULOK is seen to have a lower complexity than PSM with regard to N, because $N\log N < N^2$, whereas the complexity with regard to M and L is the same for both algorithms.

TABLE I. Complexity for the Individual Steps of the PSM Algorithm.

Operation	Complexity
Initial Fourier transform	$O(MN\log MN)$
Phase shift to Z_l	$O(LMN)$
Phase shift to $Z_l + \Delta z_l$	$O(MN^2)$
Summation over ω	$O(MN^2)$
Inverse transform (k_x)	$O(MN\log MN)$

TABLE II. Complexity of the Individual Steps of the MULOK Algorithm.

Operation	Complexity
Initial Fourier transform	$O(MN\log MN)$
Phase shift to Z_l	$O(LMN)$
Interpolation from ω to k_z	$O(LMN\log N)$
Amplitude scaling	$O(LMN)$
Inverse Fourier transform	$O(LMN \cdot \log MN)$

TABLE III. Asymptotic Complexities PSM and MULOK, Regarding N, M, and L Separately.

Algorithm	N	M	L
PSM	$O(N^2)$	$O(M\log M)$	$O(L)$
MULOK	$O(N\log N)$	$O(M\log M)$	$O(L)$

B. Empirical Evaluation of Execution Times

To do a realistic comparison of the two algorithms, several simulated processings were performed in Matlab (The MathWorks, Natick, MA). For convenience, test data sets were made using matrices with random numbers rather than actual ultrasonic scans. This should not affect the execution times of the algorithms, as they are only dependent on the size of the data sets, and not on their content. The number of measurement positions, M, was set to 128, and the processing times were measured for different number of time samples, N. The simulations were performed on a dual-core 2-GHz laptop with 2 GB of RAM, running a 64-bit Linux version of Matlab R2009b.

The resulting execution times are plotted in Fig. 3. Note that both the x- and y-axes of the plots are logarithmic. Figs. 3(a) and 3(b) show the execution times as functions of N when the number of layers L is 2 and 5, respectively. To compare the asymptotic complexities with the execution times of the simulation, lines corresponding to N^2 and $N\log N$ have been added to the plot, normalized to intersect with the execution time for the highest value of N.

We find from Figs. 3(a) and 3(b) that PSM has a lower execution time than MULOK for small values of N, but that MULOK is much faster for larger values of N. For example, for $L = 5$ and $N = 16\,384$, MULOK is approximately 15 times faster than PSM, and for $L = 2$ and $N = 16\,384$, MULOK is approximately 30 times faster. Comparing the results for $L = 2$ and $L = 5$, we see that the execution time of the PSM algorithm is approximately the same for both cases, whereas the time for the MULOK algorithm is significantly higher for $L = 5$. Thus, using a greater number of layers shifts the crossover point between the algorithms to a higher N value. The reason that MULOK is more heavily influenced by L than PSM can be found by comparing the complexities for each algorithmic step, listed in Tables I and II. PSM has only one step whose complexity is proportional to L, whereas almost all steps in MULOK have complexities proportional to L.

The execution times are seen to correspond well to the asymptotic complexities indicated by the dashed lines, particularly for larger values of N. This indicates that the

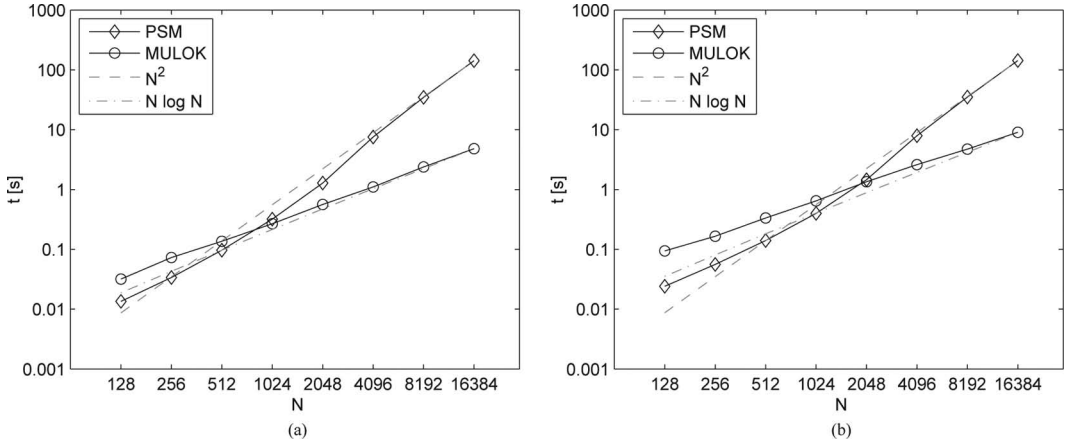

Fig. 3. Execution time simulation results: (a) $L = 2$, $M = 128$; (6) $L = 5$, $M = 128$.

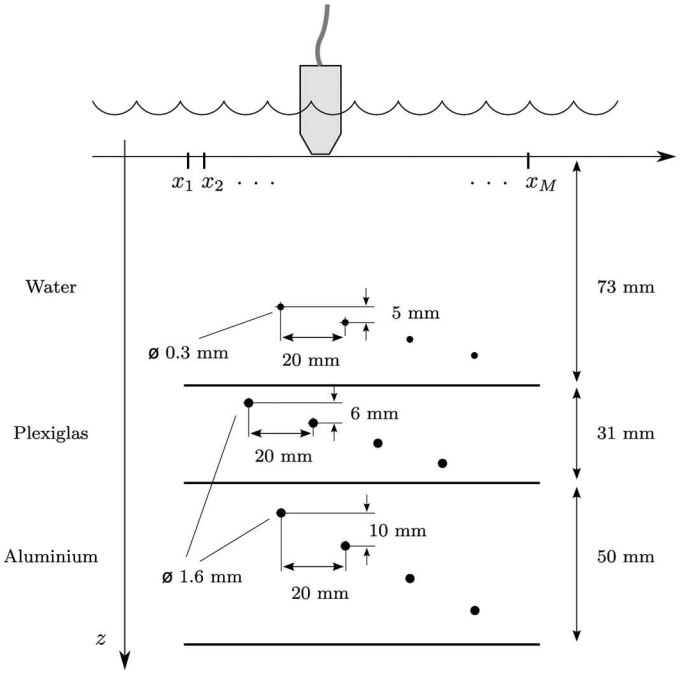

Fig. 4. Experimental setup.

general trends seen here can be assumed to be valid in general, even if the given execution times presented here are valid only for one specific implementation of the algorithms.

IV. Experiment

In Section III, it was shown that the asymptotical complexity of MULOK is lower than that of PSM with regard to N. To validate that MULOK is also capable of producing the same image quality as PSM, an experiment with a three-layer structure was conducted.

Two test blocks with side-drilled holes were placed on top of each other and immersed in a water tank, and an array of four steel pins was placed over the two blocks, as shown in Fig. 4. A B-scan of the arrangement was performed using a 2.25-MHz transducer with 6 mm diameter, moved in steps of 1 mm, with a sampling frequency of 12.5 MHz. $N = 1040$ time samples were recorded at each of the $M = 111$ measurement positions.

The upper block was 31-mm-thick poly(methyl methacrylate) (PMMA). The lower block was 50-mm-thick, aluminum. Each of the blocks had four side-drilled holes, which were all 1.6 mm in diameter and 30 mm deep. The vertical spacing between the holes was 6 mm in the PMMA block and 10 mm in the aluminum block; the horizontal spacing was 20 mm for both blocks. The blocks were also shifted horizontally approximately 10 mm, so that the upper holes would not create a dominating shadow for the lower holes. The steel pins were 0.3 mm in diameter, with a vertical spacing of 5 mm and a horizontal spacing of 20 mm. The scan line was centered over the holes and pins in the y direction.

To compensate for limited dynamic range in the ultrasonic acquisition system, a time-dependent damping/amplification was applied during the scan. The water-PMMA interface echo was damped −10 dB, and the echoes from the aluminum layer were amplified by +20 dB.

The Hilbert transform was used to create an analytic signal for each time series in the raw data, and the B-scan envelope was estimated by taking the absolute value of the analytic signal. The resulting raw data image is shown in Figs. 5(a) and 5(d) plotted with a 25 and a 50 dB dynamic range, respectively. Two different dynamic ranges were used to emphasize the difference between high-amplitude and low-amplitude effects. The front echo from the water-PMMA interface is seen as a horizontal line at approximately 100 μs, and echoes from the PMMA-aluminum and the aluminum-water interfaces are visible at approximately 123 and 137 μs, respectively.

The longitudinal wave velocities for water, PMMA, and aluminum are approximately 1480, 2730, and 6320 m/s, and the difference in velocity can be seen clearly in the B-scan, because the apparent thicknesses of the layers on the time axis are far from their actual thicknesses. The echoes from the steel pins and the side-drilled holes are seen as four reflections in each of the layers, and the width of

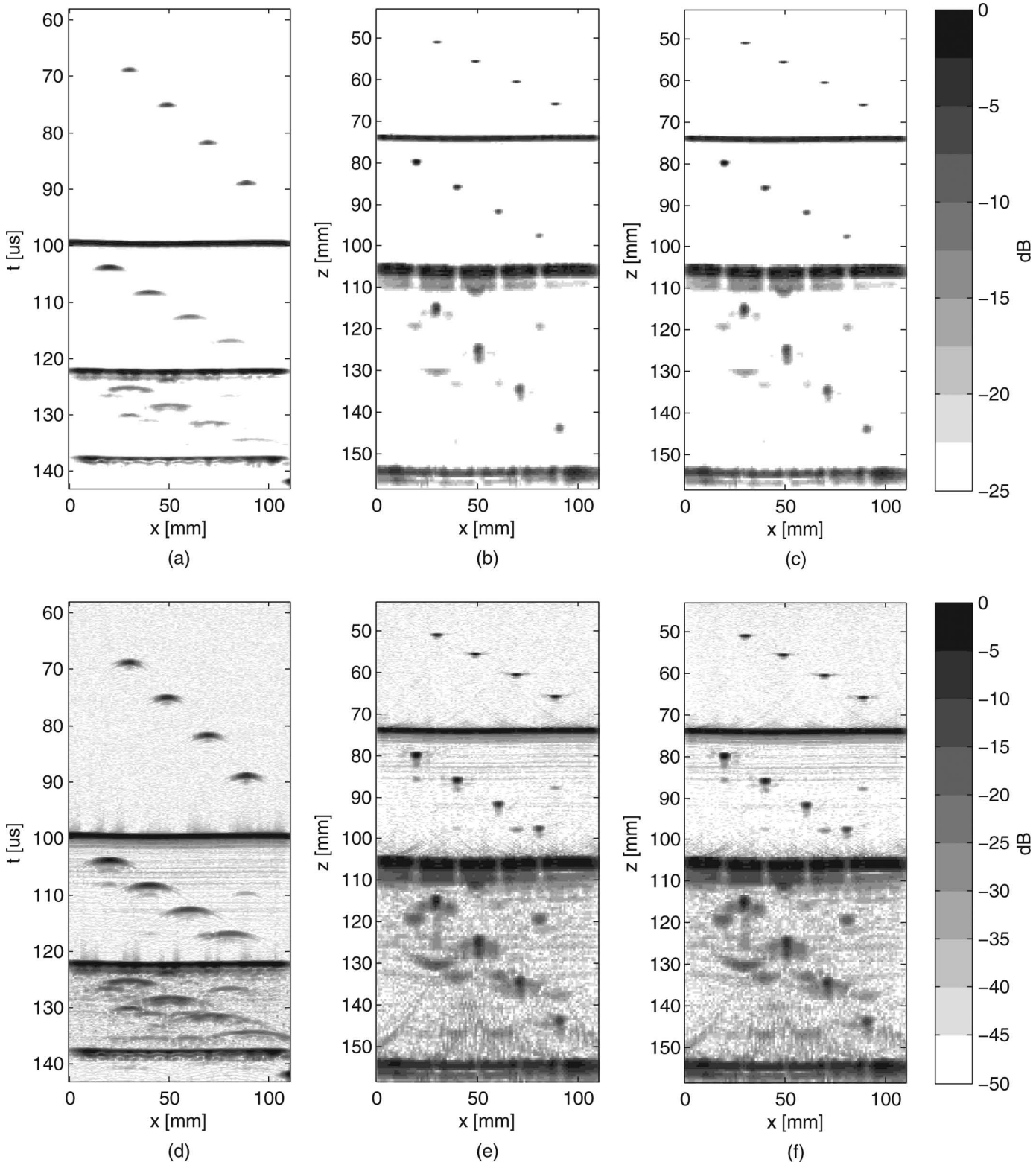

Fig. 5. Comparison of raw data and images focused by PSM and MULOK, displayed on a decibel intensity scale. The dynamic range of the top row is 25 dB: (a) raw data, (b) PSM image, (c) MULOK image; the dynamic range of the bottom row is 50 dB: (d) raw data, (e) PSM image, (f) MULOK image.

the reflections increases with depth because of the divergence of the emitted transducer pulse. There are also some weaker reflections cluttering the image in both the PMMA and aluminum layers. These are caused by multiple reflections of the scattterers.

The raw data was processed with both the MULOK and the PSM algorithms, and the resulting images are shown in Figs. 5(b), 5(c), 5(d) and 5(f), plotted with absolute value on a decibel intensity scale. Like the raw data, the images are shown with both 25 and 50 dB dynamic ranges.

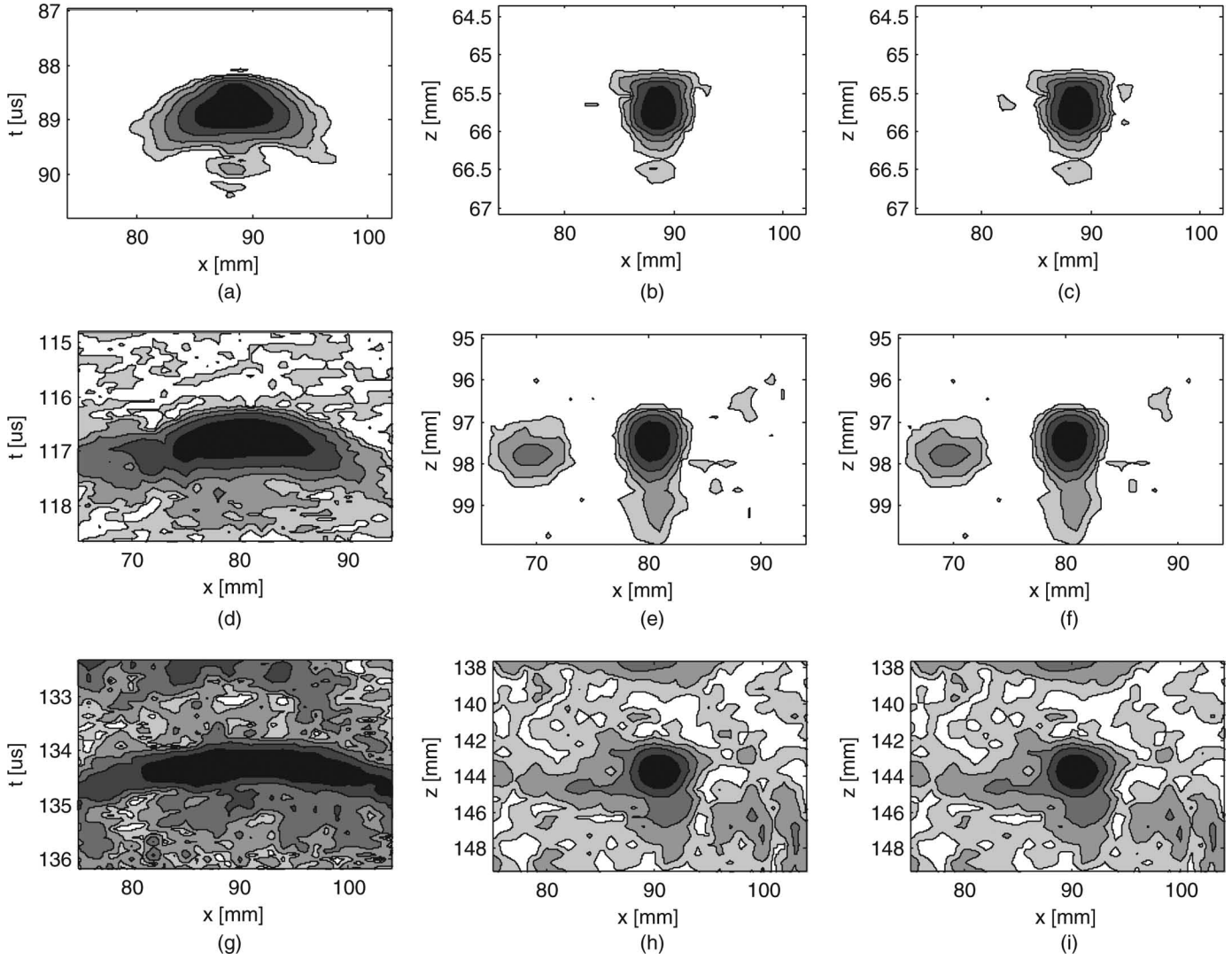

Fig. 6. Close-ups of the responses from the rightmost scatterer in each layer, interpolated to a higher resolution. Layer 1, water: (a) raw data, (b) PSM image, and (c) MULOK image. Layer 2, PMMA: (d) raw data, (e) PSM image, and (f) MULOK image. Layer 3, aluminum: (g) raw data, (h) PSM image, and (i) MULOK image. The amplitude difference between each contour is 6 dB.

It is evident from the images in Fig. 5 that the images produced by PSM and MULOK are visually very similar. The differences between PSM and MULOK will be discussed later. The reflections from the scatterers have been focused, resulting in an improved lateral horizontal resolution that is approximately the same for all scatterers, independent of depth or layer. Multiple reflections have been partially focused or defocused, depending on how close they are in time to their original scatterers. For example, the reflection seen at approximately $t = 130$ μs, $x = 30$ mm in the raw data appears to be caused by a scatterer in the aluminum layer, but it is actually a multiple reflection of the leftmost scatterer in the water layer. In the focused images, the reflection has been defocused into a curve, because it did not originate in the aluminum layer.

The improvement in lateral resolution offered by the PSM and MULOK algorithms is highlighted in Fig. 6, using close-up images of the rightmost scatterer in each layer. The extent of the z-axis in the PSM and MULOK images has been adjusted so that it covers the same depth interval as the raw B-scan image. With this compensation, we can see that the point scatterer response after focusing is quite similar for each layer. Although there is a much higher level of background noise in the aluminum layer, the high-amplitude part of the response still has approximately the same extent as for the other layers. Note also that the only visible differences between the PSM and MULOK images are within the background noise.

After close inspection of the point scatterer responses in Fig. 6, the −6-dB widths of the raw data images were found to be 6.7, 13.1, and 21.2 mm, for the water, PMMA, and aluminum layers, respectively. The corresponding −6-dB widths are 3.1, 3.1, and 3.8 mm for both the PSM and MULOK images, indicating that there is no practical difference in lateral resolution between the two algorithms. The −6-dB widths also correspond well to the theoretical resolution of approximately half the transducer diameter (3 mm), as discussed in Section II-G. The aluminum layer has a slightly broader response compared with the other

two layers, and this is probably mainly because of the higher level of background noise.

V. Discussion and Conclusions

We have presented a new algorithm for processing of ultrasonic data from multilayer structures, called MULOK, and compared it with the PSM algorithm. Both algorithms represent an extension of the SAFT concept to the case in which the imaged geometry consists of layers with differing wave velocities.

In theory, the algorithms can focus through an arbitrary number of layers. However, because the transmission factor between layers is generally less than one, both the transmitted pulse and the backscattered echo will be significantly damped at each interface. Thus, in practice, the signal-to-noise ratio is likely to limit the number of layers that can be imaged. In addition, multiple reflections from within the first layers may interfere with echoes from layers further down.

It is assumed for both the PSM and the MULOK algorithms that the layers are all horizontal. PSM can also be used to focus data from geometries in which the interfaces between layers are planar and non-horizontal, but this requires an additional processing step in which the wave field is rotated [24]. The same step can be applied to use MULOK on non-horizontal layers.

We have shown, both theoretically and by numerical simulation, that the MULOK algorithm has a lower asymptotic complexity than the PSM algorithm. However, the simulations also indicated that the effectiveness of the MULOK algorithm decreases as the number of layers increases, whereas the execution time of the PSM algorithm is more or less independent of number of layers.

We have also demonstrated that the image quality and lateral resolution is approximately the same for both algorithms. Note, however, that if the interpolation step of the MULOK algorithm is not performed accurately enough, the focused image will contain visible artifacts. Thus, the accuracy of the interpolation should be adjusted according to the image quality required. There are also variations of the ω-k algorithm which do an approximate, but efficient, mapping from ω to k_z without any interpolation, for example using the chirp z-transform [25]. Modifying MULOK to accommodate such methods is seen as a subject for future work.

Taking all factors into account, we see that the choice between PSM and MULOK relies both on the geometry to be imaged and the resources available for implementation. If the number of input samples is relatively large, the number of layers is low, and the interpolation between ω and k_z can be executed efficiently and accurately, MULOK can produce the same image quality as PSM in a much more efficient manner. If these requirements are not fulfilled, PSM may be a better alternative.

Appendix

A. Matrix Representation of Discrete Data

In Section II, the theory was outlined for the case of continuous signals, and it was also assumed that the wavefield in the measurement plane is known for all x and t. In practice, the wave field must be sampled discretely both in time and space, for a finite time period and over a finite section of the x-axis.

We assume that at each measurement position, a pulse is emitted, and N_t time samples are recorded, corresponding to time instants $t_1, t_2, \ldots, t_{N_t}$. The measurement is performed at M different x-positions, $x_1, x_2, \ldots, x_M$. Time samples are equally spaced with $\Delta T = 1/f_s$, where f_s is the sampling frequency, and the x positions are equally spaced with ΔX. Assuming that the measurement is done at depth Z_1, the discrete data set can be organized in a matrix $\mathbf{P}_{tx}[Z_1]$, with element p_{ij} corresponding to time instant t_i of the pulse-echo measurement at position x_j:

$$\mathbf{P}_{tx}[Z_1] = \begin{array}{c} \\ t_1 \\ t_2 \\ \vdots \\ t_{N_t} \end{array} \begin{array}{c} \begin{array}{cccc} x_1 & x_2 & \ldots & x_M \end{array} \\ \begin{bmatrix} p_{11} & p_{12} & \ldots & p_{1M} \\ p_{21} & p_{22} & & \vdots \\ \vdots & & \ddots & \vdots \\ p_{N_t1} & \ldots & \ldots & p_{N_tM} \end{bmatrix} \end{array}. \tag{20}$$

Note that some zero-padding of $\mathbf{P}_{tx}$ in the x-direction may be required to avoid spatial aliasing in the focused image [26]. The discrete Fourier transform of $\mathbf{P}_{tx}[Z_1]$ is also an $N_t \times M$ matrix, denoted $\hat{\mathbf{P}}_{\omega k_x}[Z_1]$. The elements of $\hat{\mathbf{P}}_{\omega k_x}[Z_1]$ correspond to ω in the range $[-\pi f_s, \pi f_s]$, but only elements that correspond to the transducer passband are significantly different from zero. Because the frequency spectra of real valued signals are symmetric, we can also limit the processing to positive ω values. Denoting the upper and lower cutoff frequency for the transducer $f_{\min}$ and $f_{\max}$, we define $\mathbf{P}_{\omega k_x}[Z_1]$ as the subset of $\hat{\mathbf{P}}_{\omega k_x}[Z_1]$ corresponding to $\omega \in 2\pi[f_{\min}, f_{\max}]$:

$$\mathbf{P}_{\omega k_x}[Z_1] = \begin{array}{c} \\ \omega_1 \\ \omega_2 \\ \vdots \\ \omega_{N_\omega} \end{array} \begin{array}{c} \begin{array}{cccc} k_{x1} & k_{x2} & \ldots & k_{xM} \end{array} \\ \begin{bmatrix} P_{11} & P_{12} & \ldots & P_{1M} \\ P_{21} & P_{22} & & \vdots \\ \vdots & & \ddots & \vdots \\ P_{N_\omega 1} & \ldots & \ldots & P_{N_\omega M} \end{bmatrix} \end{array}, \tag{21}$$

where $\omega_1 = 2\pi\big\lfloor N_t(f_{\min}/f_s)\big\rfloor$, $\omega_{N_\omega} = 2\pi\big\lfloor N_t(f_{\max}/f_s)\big\rfloor$, and the step size is $\Delta\omega = 2\pi f_s/N_t$. The relationship between N_ω and N_t is given by the ratio of transducer bandwidth to sampling frequency:

$$N_\omega/N_t \approx (f_{\max} - f_{\min})/f_s. \tag{22}$$

Also, assuming that the Fourier transform output is arranged so that the zero wavenumber is centered, and that M is even, the k_x wavenumbers are given by

$$\mathbf{k}_x = \frac{2\pi}{\Delta X \cdot M} \cdot [-M/2, -M/2+1, \ldots, 0, \ldots, M/2-1]. \tag{23}$$

B. Wave Field Extrapolation

We know from (12) and (13) that a wavefield at depth Z_l can be shifted to an arbitrary depth $Z_l + \Delta z$ within layer l by multiplication with a complex exponential $e^{ik_{zl}\Delta z}$, where k_{zl} is given by

$$k_{zl} = -\text{sgn}(\omega) \cdot \sqrt{\frac{\omega^2}{\hat{c}_l^2} - k_x^2}. \tag{24}$$

The frequency-wavenumber spectrum should be limited to propagating waves, corresponding to real-valued k_{zl}, and this requirement is fulfilled as long as the square root argument of (24) is positive. All elements of $\mathbf{P}_{\omega k_x}$ for which $(\omega^2/\hat{c}_l^2) - k_x^2 < 0$ should therefore be set to zero.

Let $\mathbf{K}_{zl}$ be the discrete matrix representation of k_{zl}. It is an $N_\omega \times M$ matrix given by

$$\mathbf{K}_{zl} = \begin{bmatrix} k_{zl}(\omega_1, k_{x1}) & \dots & k_{zl}(\omega_1, k_{xM}) \\ \vdots & \ddots & \vdots \\ k_{zl}(\omega_{N_\omega}, k_{x1}) & \dots & k_{zl}(\omega_{N_\omega}, k_{xM}) \end{bmatrix}. \tag{25}$$

The extrapolation from depth Z_l to depth $Z_l + \Delta z$ is performed with an entry-wise multiplication:

$$\mathbf{P}_{\omega k_x}[Z_l + \Delta z] = \mathbf{P}_{\omega k_x}[Z_l] \circ \exp(i\mathbf{K}_{zl}\Delta z). \tag{26}$$

C. Stolt Transformation of Variables

We know from Section II-F that the transformation from the (ω, k_x) domain to the (k_z, k_x) domain is given by

$$P(k_z, k_x, Z_l) = A_l(k_z, k_x) \cdot P_l(\omega_l(k_z, k_x), k_x, Z_l), \tag{27}$$

where

$$A_l(k_z, k_x) = \frac{\hat{c}_l}{\sqrt{1 + \frac{k_x^2}{k_{zl}^2}}}, \quad \text{and} \tag{28}$$

$$\omega_l(k_z, k_x) = -\text{sgn}(k_{zl}) \cdot \hat{c}_l \sqrt{k_x^2 + k_{zl}^2}. \tag{29}$$

The discrete version of $P(\omega, k_x, Z_l)$, $\mathbf{P}_{\omega k_x}[Z_l]$, is computed for a finite, equally spaced set of ω values. Similarly, the discrete version of $P(k_z, k_x, Z_l)$, denoted $\mathbf{P}_{k_z k_x}[Z_l]$, should be computed for an equally spaced set of k_z. However, the mapping given by $\omega_l(k_z, k_x)$ does not in general coincide with the equally spaced values of ω in $P(\omega, k_x, Z_l)$, and therefore a interpolation step is needed. The situation is illustrated in Fig. 7, where the original ω-k_x grid is indicated as black dots. For each discrete value of k_x, the spectrum has to be interpolated to a new set of ω values, indicated with gray crosses.

Using (29), we find that for a given k_{xj}, the ω values to be interpolated for are given by the vector

$$\boldsymbol{\omega}_l^{ip}(j) = \hat{c}_l \cdot \sqrt{k_{xj}^2 + \mathbf{k}_{zl}^2}, \tag{30}$$

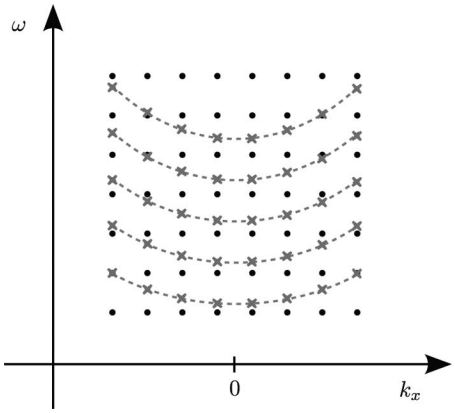

Fig. 7. Interpolation points in the ω-k_x domain.

where the sign function is omitted because only positive ω values are included in the processing. $\mathbf{k}_{zl}$ denotes the vector containing the discrete k_z values, and it is squared element by element. The interpolated values also have to be scaled according to (28), and the amplitude factors for k_{xj} are given by

$$\mathbf{a}_l(j) = \frac{\hat{c}_l}{\sqrt{1 + k_{xj}^2/\mathbf{k}_{zl}^2}}. \tag{31}$$

Assuming that all k_z values are negative, the $\mathbf{k}_{zl}$ vector is given by

$$\mathbf{k}_{z,l} = -\Delta k_{z,l} \cdot [0,1,\dots,N_{k_z} - 1]^T. \tag{32}$$

$\Delta k_{z,l}$ is the step size between each value and N_{k_z} is the total number of values; these should be chosen to cover the range of possible k_z values and also avoid any aliasing. This is fulfilled if

$$\Delta k_{z,l} \le \frac{2\pi}{\hat{c}_l} \cdot \frac{f_s}{N_t}, \tag{33}$$

and

$$N_{k_z} \ge \frac{2\pi f_{\max}/\hat{c}_l}{\Delta k_{z,l}}. \tag{34}$$

D. Algorithm Description

Fig. 8 shows the flow of the PSM and the MULOK algorithms, from the input ultrasonic data (denoted $\mathbf{P}_{tx}[Z_1]$) to the focused image (denoted $\mathbf{I}_{zx}$). $\mathbf{P}_{tx}[Z_1]$ is first Fourier transformed, and the elements corresponding to the transducer passband are extracted. Then, for each layer, the wavefield is multiplied with the phase factor $\exp\left(i\sum_{m=1}^{l-1}\mathbf{K}_{zm}d_m\right)$ to shift it from Z_1 down to the top of layer l, given by Z_l. For the first layer, the phase factor is set equal to 1, resulting in zero phase shift. The shifted wavefield is a common starting point for both algorithms, and the subsequent steps for PSM and MULOK are shown on the left and the right side of the flowchart, respectively.

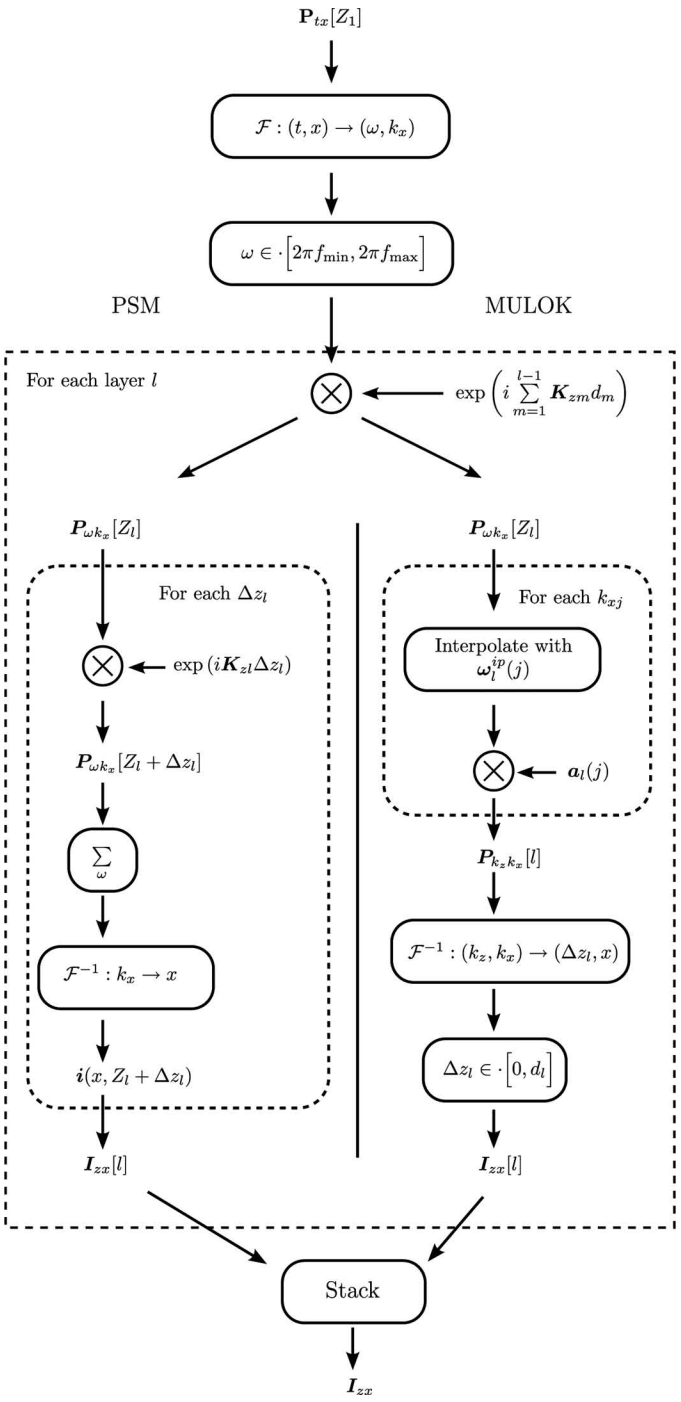

Fig. 8. Flowchart for Stolt and phase shift algorithms.

The PSM algorithm is based on forming an image line $\mathbf{i}(Z_l + \Delta z)$ for each depth to be imaged. The first operation is to compute $\mathbf{P}_{\omega k_x}[Z_l + \Delta z_l]$ by multiplying with the additional phase factor $\exp(i\mathbf{K}_{zl}\Delta z_l)$. An image line is then formed by summing over all ω and inverse Fourier transforming the resulting vector.

For the Stolt imaging algorithm, the next step after calculating $\mathbf{P}_{\omega k_x}[Z_l]$ is to interpolate from the original ω-k_x grid to the k_x-k_z grid. This is done by looping through all k_x values, interpolating for each column of $\mathbf{P}_{\omega k_x}[Z_l]$ with the ω values given by the $\boldsymbol{\omega}_l^{ip}(j)$ vector, and multiplying with the $\mathbf{a}_l(j)$ vector. Only part of the result corresponds to z values within the layer, that is, $\Delta z \in [0, d_l]$. For each layer, this part is cut out and saved as the local image $\mathbf{I}_{zz}[l]$.

When all the layers have been processed, the subimages $\mathbf{I}_{zz}[l]$ are stacked on top of each other to form the complete image of all of the layers.

E. Asymptotic Complexity

Having defined both the PSM and the MULOK implementations, it is possible to study the computational complexity of the two. Big-O notation is used to describe the growth rate of operations as function of the size of the input data. As described in part D, the raw data $\mathbf{P}_{tx}[Z_1]$ is an $N_t \times M$ matrix, corresponding to N_t time samples and M measurement positions. After Fourier transforming the data, an $N_\omega \times M$ submatrix of the result is extracted for use in the subsequent processing, where N_ω is proportional to N_t. The number of z-lines for the PSM algorithm, denoted N_z, and the number of k_z values for the MULOK algorithm, denoted N_{k_z}, are also proportional to N_t. For the sake of asymptotic complexity analysis, we can ignore all such proportionality constants, and set $N_t = N_\omega = N_z = N_{k_z} = N$. The number of layers is denoted by L.

The initial Fourier transform, from (t, x) to (ω, k_x), is a two-dimensional transform with complexity $O(MN\log MN)$. The following multiplication with a phase factor to calculate $\mathbf{P}_{\omega k_x}[Z_l]$ is an entry-wise multiplication that is performed $L - 1$ times. The complexity of this operation is thus $O(NML)$.

For the PSM algorithm, the wave field is multiplied with yet another phase factor. This multiplication is performed N times, once for each image line, and thus the complexity for all image lines is $O(MN^2)$. The summation over ω is also performed N times, resulting in a total complexity of $O(MN^2)$. Finally, the last operation is the inverse Fourier transform of an M-length vector, which is $O(MN\log M)$. The complexities of the individual steps of the PSM algorithm are summarized in Table I.

For the MULOK algorithm, the calculation of $\mathbf{P}_{\omega k_x}[Z_l]$ is followed by an interpolation step. The complexity of this step depends on the type of interpolation utilized, but in this work, the following method was used: $\mathbf{P}_{\omega k_x}[Z_l]$ was first interpolated to a denser rectangular grid by inverse Fourier transforming along the ω dimension, zero padding, and Fourier transforming back again. This operation is $O(MN\log N)$. The final interpolation was subsequently performed by linear interpolation between points on this denser grid. This operation consists of a search to find the two closest ω values and calculating a weighted sum of P for these values; the corresponding complexity is $O(MN\log N)$. Because the 2-D interpolation is performed once for each layer, the overall complexity is then $O(LMN\log N)$. Multiplication with the amplitude factors $\mathbf{a}_l(j)$ is $O(LMN)$, and the inverse Fourier transform to produce the image is $O(LMN\log MN)$. The complexities of the different steps of the MULOK algorithm are summarized in Table II.

Acknowledgments

The authors thank Prof. T. Stepinski for inviting M. H. Skjelvareid to the Signals and Systems Group at Uppsala University, where most of this research was carried out.

References

[1] R. Y. Chiao and L. J. Thomas, "Analytic evaluation of sampled aperture ultrasonic imaging techniques for NDE," *IEEE Trans. Ultrason. Ferroelectr. Freq. Control*, vol. 41, no. 4, pp. 484–493, 1994.
[2] M. Soumekh, "Array imaging with beam-steered data," *IEEE Trans. Image Process.*, vol. 1, no. 3, pp. 379–390, Jul. 1992.
[3] J. B. Bednar, "A brief history of seismic migration," *Geophysics*, vol. 70, no. 3, pp. 3MJ–20MJ, 2005.
[4] R. H. Stolt, "Migration by Fourier transform," *Geophysics*, vol. 43, no. 1, pp. 23–48, Feb. 1978.
[5] J. Gazdag, "Wave equation migration with the phase-shift method," *Geophysics*, vol. 43, no. 7, pp. 1342–1351, 1978.
[6] J. W. Goodman, *Introduction to Fourier Optics*, 2nd ed., New York, NY: McGraw-Hill, 1996.
[7] E. G. Williams, *Fourier Acoustics*. New York, NY: Academic, 1999.
[8] S. Doctor, T. Hall, and L. Reid, "SAFT—The evolution of a signal processing technology for ultrasonic testing," *NDT Int.*, vol. 19, no. 3, pp. 163–167, Jun. 1986.
[9] K. Langenberg, M. Berger, T. Kreutter, K. Mayer, and V. Schmitz, "Synthetic aperture focusing technique signal processing," *NDT Int.*, vol. 19, no. 3, pp. 177–189, Jun. 1986.
[10] K. Mayer, R. Marklein, K. Langenberg, and T. Kreutter, "Three-dimensional imaging system based on Fourier transform synthetic aperture focusing technique," *Ultrasonics*, vol. 28, pp. 241–255, Jul. 1990.
[11] L. J. Busse, "Three-dimensional imaging using a frequency-domain synthetic aperture focusing technique," in *IEEE Trans. Ultrason. Ferroelectr. Freq. Control*, vol. 39, no. 2, pp. 174–179, Mar. 1992.
[12] Y.-F. Chang and C.-C. Chern, "Frequency-wavenumber migration of ultrasonic data," *J. Nondestruct. Eval.*, vol. 19, no. 1, pp. 1–10, 2000.
[13] T. Stepinski, "An implementation of synthetic aperture focusing technique in frequency domain," *IEEE Trans. Ultrason. Ferroelectr. Freq. Control*, vol. 54, no. 7, pp. 1399–1408, Jul. 2007.
[14] N. Pörtzgen, D. Gisolf, and G. Blacquière, "Inverse wave field extrapolation: A different NDI approach to imaging defects," *IEEE Trans. Ultrason. Ferroelectr. Freq. Control*, vol. 54, no. 1, pp. 118–127, Jan. 2007.
[15] A. J. Hunter, B. W. Drinkwater, and P. D. Wilcox, "The wavenumber algorithm for full-matrix imaging using an ultrasonic array," *IEEE Trans. Ultrason. Ferroelectr. Freq. Control*, vol. 55, no. 11, pp. 2450–2462, Nov. 2008.
[16] M. A. Haun, D. L. Jones, and W. D. O'Brien, Jr., "Adaptive focusing through layered media using the geophysical "time migration" concept," in *2002 IEEE Ultrasonics Symp.*, vol. 2, pp. 1635–1638.
[17] M. H. Skjelvareid and Y. Birkelund, "Ultrasound imaging using multilayer synthetic aperture focusing," in *ASME 2010 Pressure Vessels and Piping Conf.*, vol. 5, pp. 379–387.
[18] T. Olofsson, "Phase shift migration for imaging layered objects and objects immersed in water," *IEEE Trans. Ultrason. Ferroelectr. Freq. Control*, vol. 57, no. 11, pp. 2522–2530, Nov. 2010.
[19] Y. C. Kim, R. Gonzalez, and J. R. Berryhill, "Recursive wavenumber-frequency migration," *Geophysics*, vol. 54, no. 3, pp. 319–329, Mar. 1989.
[20] J. F. Claerbout, *Imaging the Earth's Interior*. Cambridge, MA: Blackwell Scientific Publications, 1985.
[21] G. M. Margrave, *Numerical Methods in Exploration Seismology—With Algorithms in MATLAB*. University of Calgary, 2003, [Online]. Available: http://www.crewes.org/ResearchLinks/FreeSoftware/NumMeth.pdf
[22] L. Brekhovskikh and O. Godin, *Acoustics of Layered Media I: Plane and Quasi-Plane Waves*, Springer Series on Wave Phenomena. New York, NY: Springer-Verlag, 1990.
[23] P. T. Gough and D. W. Hawkins, "Unified framework for modern synthetic aperture imaging algorithms," *Int. J. Imaging Syst. Technol.*, vol. 8, no. 4, pp. 343–358, 1998.
[24] T. Olofsson, M. H. Skjelvareid, and A. Barkefors, "Ultrasonic imaging of immersed objects using migration techniques," in *European Conf. Synthetic Aperture Radar 2010*, 2010, pp. 442–445.
[25] R. Lanari, "A new method for the compensation of the SAR range cell migration based on the chirp z-transform," *IEEE Trans. Geosci. Rem. Sens.*, vol. 33, no. 5, pp. 1296–1299, 1995.
[26] K. Gu, J. Wang, and J. Li, "Migration based SAR imaging for ground penetrating radar systems," in *IEE Proc. Radar, Sonar Navig.*, vol. 151, no. 5, Oct. 2004.

Martin H. Skjelvareid (S'09) was born 1982 in Steigen, Norway. He received his M.Sc. degree in electronics and acoustics from the Norwegian University of Science and Technology in 2008, and is currently a Ph.D. degree candidate at the University of Tromsø, Norway. He is also employed at Breivoll Inspection Technologies, where he is working on methods for inline pipeline inspection using ultrasound. His current research interests include ultrasonic thickness gauging, ultrasonic imaging, and signal processing.

Tomas Olofsson was born 1968 in Sandviken, Sweden. He received his M.Sc. degree in engineering physics in 1994 and his Ph.D. degree in signal processing in 2000, both from Uppsala University. He is currently working as an associate professor in the Signals and Systems group, Uppsala University, Sweden. His research concerns inference problems, in particular inverse problems in ultrasonics.

Yngve Birkelund (S'99–M'03) received the M.Sc. degree in electrical engineering and the Ph.D. degree in physics from the Department of Physics and Technology, at the University of Tromsø, Norway, in 1999 and 2003, respectively. Dr. Birkelund joined the Faculty of Engineering and Economics, Tromsø, University College, in 2003 as an Associate Professor, and became the head of the Control System Bachelor Program in 2004. In 2007, he returned to his current position at the University of Tromsø, Tromsø, Norway, as an Associate Professor in the Department of Physics and Technology. His area of research include signal processing, statistics, non-linear dynamics, systems identification, time- frequency analysis, microwaves techonology for medical applications and ultrasonics for non-destructive testing.

Yngvar Larsen (S'00–M'04) received the M.Sc. degree in applied physics and the Ph.D. degree in physics from the University of Tromsø, Tromsø, Norway, in 1999 and 2003, respectively. During the summer of 1999, he was a Research Assistant with the NATO SACLANT Undersea Research Centre, La Spezia, Italy. From July 2001 to June 2002, he was a Visiting Researcher with the University of Minnesota, Minneapolis, MN. He is currently a Senior Researcher with Norut. His current research interests include signal processing for SAR, particularly the applications of interferometric SAR.